Volume 12
Number 33
7 September 2024
Pages 21471–22326

Journal of Materials Chemistry A

Materials for energy and sustainability

rsc.li/materials-a

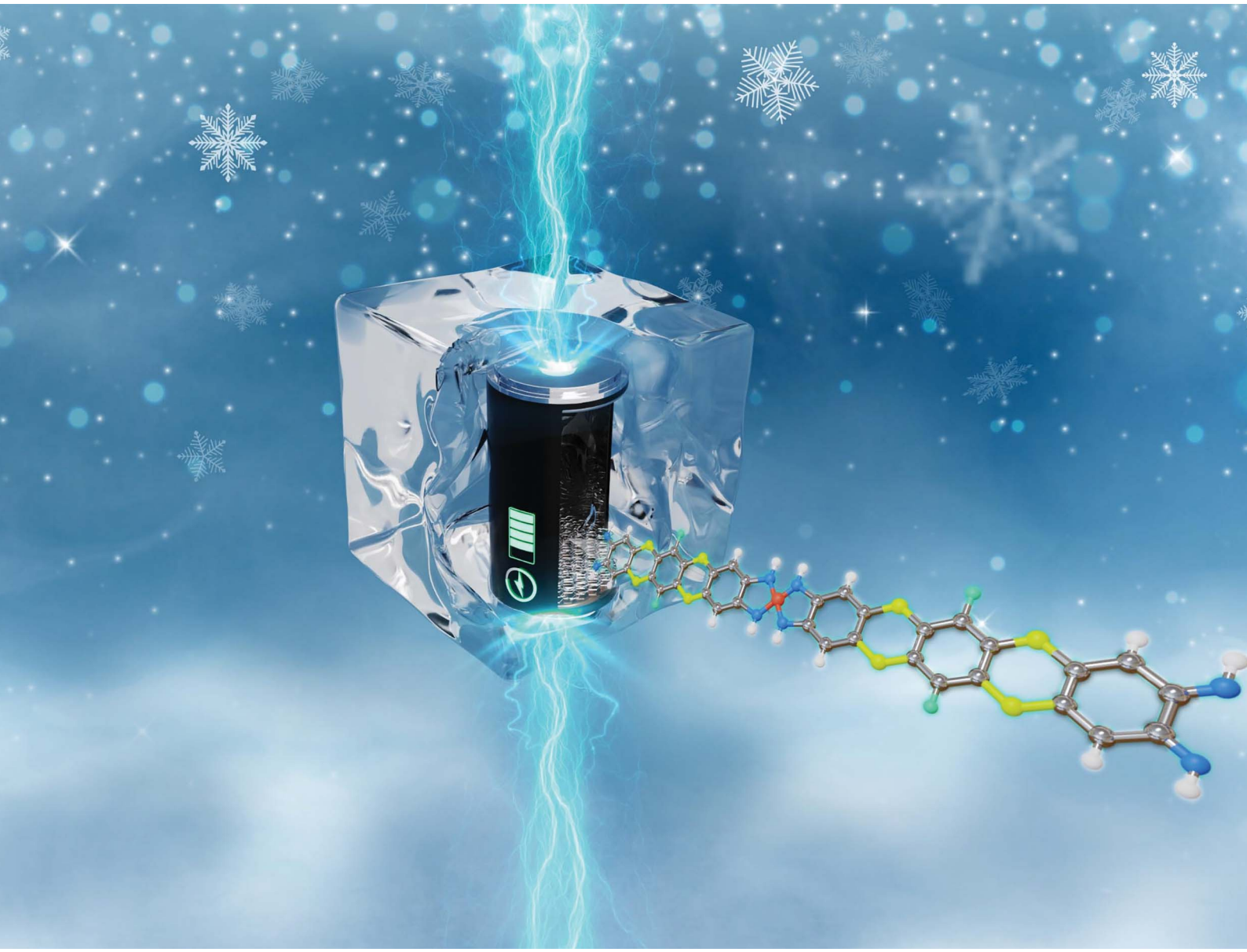

ISSN 2050-7488

ROYAL SOCIETY OF CHEMISTRY

PAPER

Kanghoon Yim, Jungjoon Yoo, Hyunuk Kim *et al.*
Redox-active conductive metal–organic framework with high lithium capacities at low temperatures

Journal of Materials Chemistry A

ROYAL SOCIETY OF CHEMISTRY

PAPER

View Article Online
View Journal | View Issue

Check for updates

Cite this: J. Mater. Chem. A, 2024, 12, 21732

Redox-active conductive metal–organic framework with high lithium capacities at low temperatures†

Yogendra Kumar,‡[a] Tae Hyeong Kim,‡[b] Iyan Subiyanto,[ac] Winda Devina,[a] Segi Byun,[a] Subhajit Nandy,[d] Keun Hwa Chae,[d] Suim Lim,[e] Bumjin Kim,[b] Sanghui Kang,[b] Seong Ok Han,[a] Kanghoon Yim,*[e] Jungjoon Yoo*[b] and Hyunuk Kim*[ac]

Received 16th March 2024
Accepted 11th July 2024

DOI: 10.1039/d4ta01779j

rsc.li/materials-a

Lithium-ion batteries suffer from reduced capacities and stabilities at low temperature due to poor Li intercalation to the graphite anode. Graphite has a high activation energy (~0.6 eV) to accommodate Li ions, resulting in a substantial capacity drop at low temperatures. Additionally, it can induce the formation of Li dendrites on the surface of graphite. To address this issue, we designed and synthesized a redox-active fluorothianthrene-based MOF (SKIER-5). SKIER-5, which undergoes three-electron redox reactions resulting from the fluorothianthrene-based organic ligand and Ni, exhibited excellent electrochemical performance at various temperatures when used as an anode. In particular, the discharge capacities of SKIER-5 were significantly higher than those of commercial graphite at low temperatures (<−10 °C) because of the lower activation energy (~0.23 eV) for charge transfer. Moreover, it maintained stability when cycled at −20 °C, highlighting its potential as a promising anode material in low-temperature environments.

Introduction

The search for novel redox-active conductive metal–organic frameworks (RC-MOFs) constructed from metal ions and conjugated organic ligands has received considerable attention because of recent interest in energy storage.[1,2] MOFs have a well-defined periodic structure, making them excellent electrodes for storing ions in their pores.[3] Most MOFs, however, have poor electrical conductivity because of their wide HOMO–LUMO gaps, hindering their use as electrode materials.[4] Only a few MOFs with excellent electronic conductivity have been reported as electrode materials.[5] Furthermore, MOFs, composed of both metal ions and organic ligands, with favorable redox properties have seldom been developed to enhance energy storage.[6] For example, TAB-based 1D MOFs were easily synthesized by a one-pot reaction and used as anode materials for LIBs.[6,7] Ni(TIB) showed a specific capacity of 193 mA h g^{-1} at a current rate of 50 mA g^{-1} (after the 40th cycle) with excellent stability (more than 1000 cycles).

Lithium-ion batteries (LIBs) have dominated the secondary battery market because of their high energy density and good cycling stability.[8,9] Despite significant advancements, however, traditional LIBs still suffer from low rate capability, poor capacity and sluggish charging behavior due to slow electron transfer and ion diffusion processes at low temperatures.[10] Commercial LIBs use lithium transition metal oxide as the cathode and graphite as the anode. Graphite has a high activation energy (~0.6 eV) to accommodate Li ions, resulting in a substantial capacity drop at low temperatures.[11] Additionally, it can induce the formation of Li dendrites on the surface of graphite. Therefore, significant efforts have been devoted to exploring novel anode materials for LIBs that function at low temperatures.[12]

To address this issue, we designed a fluoro-thianthrene (TATH)-based RC-MOF with three-electron redox properties as a result of the presence of both TATH and Ni. Heteroatom (F, S, O, N)-based π-conjugated ligands can provide additional lithium ion binding sites during charge/discharge cycles of LIBs[13–15] and result in high electrical conductivity.[16–18] Herein, we report the synthesis and characterization of a fluoro-

[a]Hydrogen Convergence Materials Laboratory, Korea Institute of Energy Research, 152 Gajeong-ro, Yuseong-gu, Daejeon 34129, Republic of Korea. E-mail: hyunuk@kier.re.kr
[b]Energy Storage Research Department, Korea Institute of Energy Research, 152 Gajeong-ro, Yuseong-gu, Daejeon, 34129, Republic of Korea. E-mail: jjyoo@kier.re.kr
[c]Energy Engineering, University of Science and Technology, 217 Gajeong-ro, Yuseong-gu, Daejeon, 34113, Republic of Korea
[d]Advanced Analysis Center, Korea Institute of Science and Technology, 5, Hwarang-ro 14-gil, Seongbuk-gu, Seoul, 02792, Republic of Korea
[e]Energy AI & Computational Science Laboratory, Korea Institute of Energy Research, 152 Gajeong-ro, Yuseong-gu, Daejeon 34129, Republic of Korea. E-mail: khyim@kier.re.kr

† Electronic supplementary information (ESI) available. See DOI: https://doi.org/10.1039/d4ta01779j

‡ These authors contributed equally.

thianthrene-based 1D RC-MOF, Ni(TATH) (denoted SKIER-5), and its excellent electrical properties as an anode at various temperatures. Notably, the capacity of SKIER-5 is significantly superior to that of commercial graphite at low temperatures (<−10 °C). In particular, the discharge capacity (150.30 mA h g^{-1}) of SKIER-5 is ∼5 times higher than that (28.58 mA h g^{-1}) of commercial graphite at −20 °C because of its low activation energy (∼0.23 eV). After 180 cycles at 0.2C and −20 °C, SKIER-5 retains a specific capacity as high as 163 mA h g^{-1}, with no capacity degradation. This represents, to the best of our knowledge, the first example of a low-temperature RC-MOF anode.

Experimental

Materials and methods

The chemicals used were purchased from Sigma-Aldrich, TCI, Alfa Aesar or Arcos Organic and used as received. Difluorobenzo [5,6][1,4]dithio[2,3-*b*]thianthrene was prepared by reported methods.[19] Thin-layer chromatography (TLC) was carried out on aluminum plates coated with silica gel mixed with fluorescent indicator and sourced from Merck, Germany. ^{1}H and ^{13}C NMR spectra were recorded on a Bruker 600 MHz spectrometer in $CDCl_3$ with TMS as a standard. Spin multiplicities are reported as singlet (s), doublet (d), and triplet (t) with coupling constants (*J*) given in Hz or multiplet (m). Solid-state NMR data were obtained from a 500 MHz Avance III HD Bruker Solid-state NMR. HRMS-ESI spectral data were obtained using the AB SCIEX TripleTOF® 5600 plus system high definition mass spectrometer. XRD data were collected using a Bruker D8 ADVANCE diffractometer with Cu $K_{\alpha1}$ radiation. Fourier transform-infrared (FT-IR) spectra in neat and *in situ* FT-IR spectra were recorded using a Thermo Scientific™ Nicolet™ iS™ 50 and iN10MX FT-IR spectrometer, respectively. XPS measurements were carried out using (K-alpha, Thermo VG Scientific) with a monochoromatized Al K-alpha source under a high vacuum condition of 7×10^{-8} Torr. SEM images were taken using a Hitachi SU8000 field emission scanning electron microscope (FE-SEM). Images were acquired in secondary electron mode at 20 kV accelerating voltage and at a working distance of 8–10 mm. TEM experiments were carried out using a Cryo Field Emission TEM (Glacios, Thermo Fisher) instrument at 200 kV. Electrical conductivity was measured *via* a 4-probe method by applying an appropriate pressure without applying any unique paste (CMT-SR2000N).

Synthesis of TATH. The synthetic scheme is described in Fig. S1.† A THF solution (10 mL) of compound 3 (0.219 g, 0.17 mmol) was added to a 2.0 M aqueous HCl solution (0.5 mL, 1.0 mmol), the mixture was stirred at room temperature for 30 minutes and a precipitate formed. The precipitate was isolated by centrifugation, washed with hexane (5.0 mL × 3), and dried under vacuum to give TATH (0.02 g, 0.04 mmol) as a light yellow solid in 83% yield. ^{1}H NMR (DMSO-d^6): δ (ppm) 7.25 (s, 4H, phenylene CH). The synthesis and characterizations of all compounds are described in the ESI (Fig. S2–S6†).

Synthesis of SKIER-5. A solution of 731.66 mg (2.5 mmol) of nickel acetate hexahydrate ($Ni(OAc)_2.6H_2O$) in 10 mL of DMF was added to a TATH (380 mg, 0.637 mmol) solution in 10 mL of DMF. Concentrated aqueous ammonia (200 μL) was added, and the mixture was stirred in air at 65–70 °C overnight. A dark cyan precipitate was obtained and separated *via* centrifugation, and the solid was extensively washed three times with water and acetone. The cyan solid powder was then dried under vacuum at 100 °C overnight. Yield: 180 mg (30%), solid-state ^{13}C NMR: δ (ppm) 153.34, 158.49, 134.44, 126.90, 119.61 (Fig. S7†).

Characterization techniques

Electrochemistry. Working electrodes were prepared from SKIER-5 (active materials). Super P and poly(vinylidene difluoride) at a mass ratio of 47 : 50 : 3 were thoroughly mixed with N-methyl-2-pyrrolidone to form a homogeneous slurry, which was then cast onto copper foil with the help of a doctor blade and dried overnight at 100 °C under vacuum.[18,20–27] The composite mass loading was approximately 1.2 mg cm^{-2}. The graphite electrode was fabricated from active material, Super P, and poly(vinylidene difluoride) at a mass ratio of 80 : 10 : 10 or 47 : 50 : 3, thoroughly mixed with N-methyl-2-pyrrolidone to form a slurry, which was then coated on copper foil and dried overnight at 100 °C under vacuum. The composite mass loading was approximately 1.1 mg cm^{-2}. CR2032-type coin cells were assembled in an Ar-filled glove box. A lithium foil was used as the counter electrode, a 1 M $LiPF_6$ solution in a 1 : 1 v/v mixture of ethylene carbonate and dimethyl carbonate (EC/DMC, anhydrous, Sigma-Aldrich) was used as the electrolyte, and a glass fiber (Whatman GF/B) was used as the separator. For all cells, cycling was started with discharging unless stated explicitly. The CV study was recorded with a BioLogic VSP potentiostat and with EC-Lab software over the voltage range 0.01–3.0 V (*vs.* Li/Li^+), and EIS data were recorded with a Bio-Logic VSP potentiostat over a frequency range of 10 mHz to 1 MHz. Galvanostatic discharge–charge experiments were conducted with a Maccor series 4000 (Maccor Co. Ltd) at a constant temperature of 25 °C, as well as at various temperatures ranging from 25 °C to −20 °C for low-temperature testing, and over the voltage range 0.01–3.0 V. The temperature and humidity chamber (JeioTech, Inc.) was used to provide different temperature ranges for above measurement.

X-ray absorption fine structure (XAFS). Ni K-edge XAFS measurements were carried out at room temperature for the Ni plate, NiO, and SKIER-5 at the 1D KIST-PAL beamline in the Pohang Accelerator Laboratory,[11] South Korea. Si (111) double crystal monochromators were used to select energy with an energy resolution of $\Delta E/E$ of 10^{-4} from a broad energy range (4–20 keV). The electron storage ring at PAL was operated at an energy of 3 GeV with a beam current of 300 mA. Higher harmonics were suppressed by detuning the monochromators to reduce the intensity of the incident beam by 60%. The as-obtained XAFS data were processed and analyzed using IFEFFIT software packages in the Athena module.[28] Pre-edge and postedge background subtraction from the overall absorption spectra and normalization were performed using the Athena module. Extended X-ray absorption fine structure (EXAFS) simulations were performed using IFEFFIT software packages in the Artemis module.[29]

Near edge X-ray absorption fine structure (NEXAFS). Ni $L_{2,3}$ edge NEXAFS measurements were carried out on SKIER-5 in the 1st and 2nd charging and discharging states at room temperature under ultrahigh vacuum (3×10^{-9} Torr). These measurements were performed using total electron yield (TEY) mode at the 10D XAS-KIST beamline in Pohang Accelerator Laboratory, South Korea. This beamline was designed to work at low energies ranging from 100–1500 eV. Grating 3 with 1000 lines/mm was used for Ni $L_{2,3}$ edge measurements with energies ranging between 850–885 eV. Background subtraction and normalization were performed with respect to the postedge height of the as-obtained spectra. Deconvolution of the Ni L_2 and L_3 peaks into t_{2g} and e_g was achieved using the Gaussian + Lorentzian area profile in peak fit software.

Theoretical calculations. Geometry optimization for SKIER-5 was carried out *via* density functional theory (DFT) calculations using the Vienna *ab initio* Simulation Package (VASP).[30] We employ the generalized gradient approximation (GGA)[31] for the exchange-correlation functionals and the DFT-D3 method[32] for van der Waals interactions. The energy cutoff for the plane-wave basis set was set to 450 eV, and the *k*-point sampling was set to a gamma-only point that satisfies the convergence criteria of E/atom < 0.01 eV and pressure < 10 kBar. In addition, we applied the on-site Hubbard interaction energy of U–$J = 6.4$ eV on nickel ions using the DFT + U method[33] to correct the poor description of the conventional GGA approach on 3d electrons. To determine the crystal structure of SKIER-5, we searched various cell sizes with different numbers of Ni(TATH) units and found that a structure with 3×2 units per cell produced the most consistent XRD peaks compared to the experiment. Starting with the lattice parameters obtained by Pawley refinement, we further fully optimized the crystal structures and confirmed that the structure was well maintained with a stacking energy of −2.41 eV per oligomer. Since conventional DFT usually underestimates the band gap, we calculated the band gap of SKIER-5 using the HSE06 hybrid functional following the efficient scheme proposed by Y. Youn *et al.*[34] The Li-binding energy ($E_{\mathrm{bind}}(\mathrm{Li}_x)$)is calculated by the equation

$$E_{\mathrm{bind}}(\mathrm{Li}_x) = \frac{E_{\mathrm{tot}}(\mathrm{Li}_x) - E_{\mathrm{tot}}(\mathrm{Li}_{x-1})}{E(\mathrm{Li})} \quad (1)$$

where $E_{\mathrm{tot}}(\mathrm{Li}_x)$ is the total free energy of SKIER-5 containing x Li atoms and E(Li) is the energy of Li metal per atom. To predict theoretical capacity, we add six Li atoms (one Li per oligomer) at a time, until the averaged Li-binding energy become positive.

For calculations Ni(TATH) model molecules, we used Gaussian 16 package for the DFT calculation to optimized the molecular structures and calculate the LUMO level. We use B3LYP exchange-correlation functional and 6-31g(d) for the basis set.

Results and discussion

Synthesis and materials characterization

SKIER-5 was synthesized through one-pot synthesis from 6,13-difluorobenzo[5,6][1,4]dithio[2,3-*b*]thianthrene-2,3,9,10-tetraamine (TATH) and Ni(II) in the presence of DMF. The basicity of the solvothermal reaction was controlled by adding ammonia solution (Fig. 1a). The precursor solution was heated overnight at 65 °C. As a result of the coordination of deprotonated TATH to Ni(II), the solution color changed to dark cyan during the reaction (Fig. S8†). The dark cyan precipitate was separated by centrifugation after an overnight reaction. It was then washed three times with water and acetone before being vacuum-dried (Fig. S9†). The final crystalline product was obtained in 30% yield.

The powder X-ray diffraction (PXRD) analysis of SKIER-5 showed a crystalline phase with distinctive peaks at $2\theta = 8.5°$, 13.7°, 21.2°, 23.9°, 25.6°, 27.0°, and 43.0° (Fig. 1b). The density functional theory (DFT) simulation of the plausible Ni(II) and TATH coordination models demonstrated that the 1D structure of SKIER-5 was in the *P*1 space group, with lattice parameters of $a = 18.3083$ Å, $b = 13.0655$ Å, $c = 20.1072$ Å, $\alpha = 95.8843°$, $\beta = 34.5212°$, $\gamma = 91.8878°$ (Fig. 1c). The unit cell parameters were refined using a Pawley fit based on the experimental PXRD profile.[35] The R_{wp} value of 3.39 percent indicated that the 1D MOF structure is consistent with the DFT model. TATH coordinated to Ni(II) in a square planar manner, with a coordination bond involving the d orbital of Ni(II) and the delocalized π orbital of the tetra-amine ligands. As a result, the zig-zag structure of TATH flattened, enabling π–π stacking of the molecules (Fig. 1c). The electronic structure of SKIER-5 determined by DFT calculations was consistent with semiconducting properties and a narrow band gap (0.37 eV) (Fig. 1d).[34,36,37] The band gap of 0.37 eV indicated a high carrier concentration, which contributed to the high electric conductivity. The electrical conductivity of SKIER-5 with a π-d conjugated system was measured *via* a four-probe device to be 8 μS m^{-1} at room temperature. This value was consistent with that of reported conductive MOFs.[6,36]

Scanning electron microscopy (SEM) and transmission electron microscopy (TEM) images revealed that SKIER-5 adopted a rod-shaped morphology with a length of ∼1 μm and a thickness of 200–300 nm (Fig. 1e and S10†). According to the Bravais-Friedel-Donnay-Harker (BFDH) law,[28,38,39] this rod-shaped morphology could be the result of π–π intermolecular interactions between the TATH molecules.[6] The results of TEM energy dispersive spectroscopy (EDS) suggested that all constituent elements of SKIER-5 were uniformly distributed over the crystals, indicating that the crystals were in a periodic crystalline phase. In particular, Ni was homogenously colocated with organic ligands in the crystals. The BET surface area of SKIER-5 determined from the N_2 sorption isotherm at 77 K was 23.195 m^2 g^{-1} (Fig. S11†).

Ni K-edge X-ray absorption spectroscopy experiments were performed to determine the local structure of the coordination bonds. The normalized X-ray absorption near edge structure (XANES) spectra of SKIER-5 clearly revealed a shoulder peak at 8340 eV, which was attributed to the Ni(II) oxidation state and square planar configuration (Fig. 1f). Furthermore, two distinct peaks at 855.17 eV and 873.29 eV for Ni 2p3/2 and Ni 2p1/2 in the XPS data confirmed the oxidation state of Ni(II) (Fig. 1g and S12†). Extended X-ray absorption fine structure (EXAFS) measurements of SKIER-5 revealed Ni–N and Ni–Ni interactive

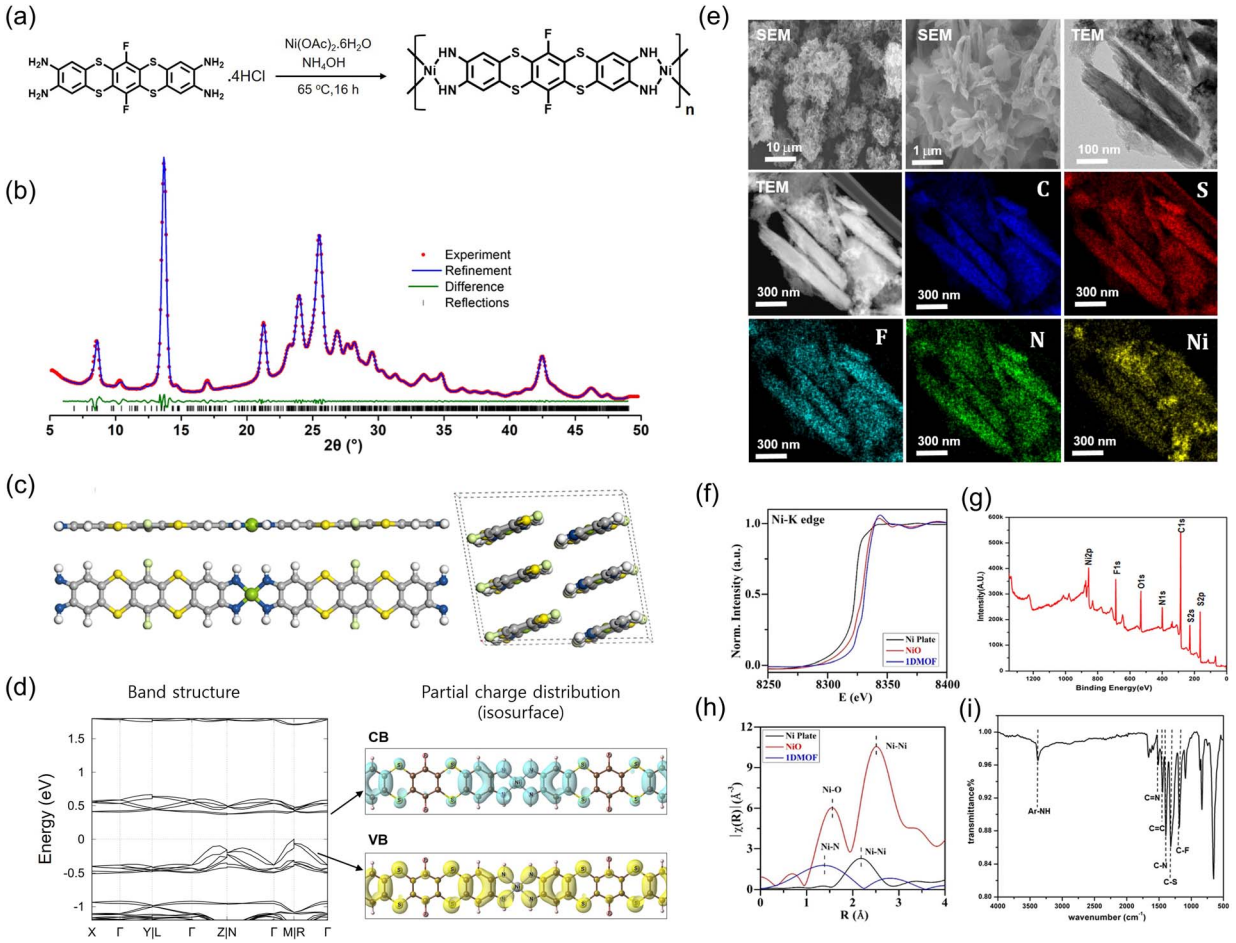

Fig. 1 Synthesis and characterization of SKIER-5. (a) Schematic of the SKIER-5 synthesis. (b) X-ray powder diffraction patterns for SKIER-5 refined with the reference profile. (c) Crystal structure of SKIER-5 optimized with DFT simulations. (d) Simulated band structure of SKIER-5. (e) SEM, TEM and EDS mapping images of SKIER-5. (f) Ni K-edge XANES spectra of SKIER-5 with those of reference materials, which confirmed the presence of Ni^{2+}. (g) XPS spectra of SKIER-5, showing the presence of only Ni, O, N, S, F. (h) EXAFS spectra revealing the coordination bonds of nickel. (i) FT-IR spectra of SKIER-5, exhibiting the bond lengths b/w the elements.

shells. As a result, the coordination number and bond distance of the Ni–N shell were 4.2 and 2.143 Å, respectively, demonstrating the square planar configuration of SKIER-5 (Fig. 1h and S13, Table S1†). Two N 1 s peaks at 399.6 and 397.9 eV, corresponding to anilinic amine (–NH–) and quinoid imine (=NH–), also supported a coordination bond between Ni(II) and deprotonated TATH (Fig. S5b†). FT-IR and solid-state magic angle spinning NMR data were used to further characterize the TATH ligand in SKIER-5 (Fig. 1i and S7†).

Electrochemical properties of SKIER-5

The performance of SKIER-5 as an anode material was investigated in a half-cell configuration (CR-2032) using lithium foil as both the counter and reference electrodes and 1.0 M $LiPF_6$ in ethylene carbonate and dimethyl carbonate (DMC) (1 : 1 volume ratio) as the electrolyte. Cyclic voltammetry (CV) curves of SKIER-5 were measured at a scan rate of 0.1 mV s^{-1} in the voltage range of 0.01 to 3.0 V *vs.* Li/Li^+ (Fig. 2a). In the initial cycle, three cathodic peaks at 0.74 V, 1.15 V, and 1.4 V were observed. The peak at approximately 0.74 V was attributed to the SEI layer formed by the decomposition of the electrolyte, while the peaks at 1.15 and 1.4 V were assigned to Li^+ insertion into the SKIER-5.[13] These cathodic peaks almost disappeared in the subsequent cycles, indicating that the lithiation of SKIER-5 was only semireversible. For the anodic process, three small peaks were observed at 0.96 V, 1.3 V and 2.4 V, which were attributed to the delithiation of SKIER-5. After the second cycle, the subsequent CV curves showed no substantial change, demonstrating stable and superior reversibility.

We performed galvanostatic discharge–charge tests of SKIER-5 for the selected cycles (1st, 2nd, 5th, 8th and 10th) at a current density of 113 mA g^{-1} (0.2C) (Fig. 2b). The SKIER-5 electrodes exhibited initial discharge and charge capacities of 713 mA h g^{-1} and 478 mA h g^{-1}, respectively. Thus, the irreversible capacity was 235 mA h g^{-1} with ~67% coulombic efficiency in the initial cycle, which was mainly attributed to electrolyte decomposition with the formation of a solid electrolyte interphase (SEI) film and incomplete conversion reaction. This phenomenon is very common in most MOFs used as

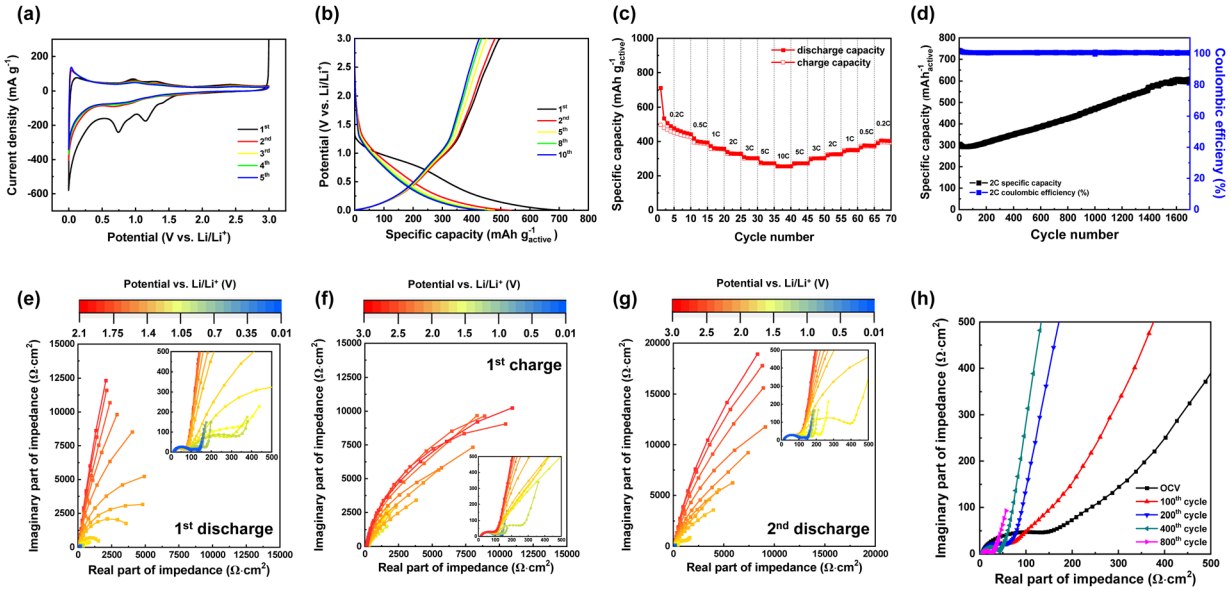

Fig. 2 Electrochemical behavior of SKIER-5 in the voltage range 0.01–3.0 V *vs.* Li/Li$^+$. (a) CV curves for different cycles at a scanning rate of 0.1 mV s^{-1}. (b) Charge–discharge curves for different cycles at 113 mA g^{-1}. (c) Rate capabilities at various current rates. (d) Cycling stability and coulombic efficiency at 200 mA g^{-1}. Impedance spectra of the SKIER-5 electrode during the (e) 1st discharge, (f) 1st charge, and (g) 2nd discharge. (h) Nyquist plot for different cycles.

anode materials.[40] However, the SKIER-5 electrode exhibited reversible reactions for stable lithium storage from the second cycle, consistent with the CV results shown in Fig. 2a. The rate capability of SKIER-5 was evaluated at different C-rates (Fig. 2c). SKIER-5 delivered specific discharge capacities of 443, 394, 358, 329, 303, 274, and 256 mA h g^{-1} during the 5th cycle at current rates of 0.2, 0.5, 1, 2, 5, and 10C, respectively. When the current density returned to 0.2C after 70 cycles, the capacity recovered to 394 mA h g^{-1} with 98% coulombic efficiency. When the cycling performance of SKIER-5 was tested at a current density of 200 mA g^{-1}, the capacity markedly increased during the cycling test. After 1600 cycles, the discharge capacity reached 600 mA h g^{-1}, comparable or superior to those of MOFs used in lithium-ion batteries (Fig. 2d, Table S2 and S3†). The slow capacity increase in Fig. 2d may be attributed to the gradual activation of the electrode materials. During the charging and discharging process, binding sites become more active and better able to accept Li ions. This phenomenon was often observed in micro-to-nanostructured anodes, where the activation of the electrolyte-derived surface layer or defects can contribute to increased capacity.[41–43] To evaluate this hypothesis, the increase in active sites during charging/discharging was monitored using staircase potentiostatic electrochemical impedance spectroscopy (SPEIS). In the initial state (open-circuit voltage 2.1 V), the Nyquist plot of a SKIER-5 half-cell exhibited a high-frequency semicircle attributed to charge transfer at the lithium metal anode, and a segment of a much larger low-frequency semicircle associated with the high charge transfer resistance of SKIER-5 (Fig. 2e).[6] As the potential was slowly decreased, particularly below 1.7 V, the radius of this low-frequency semicircle was reduced significantly, indicating a decrease in the active material charge transfer resistance (Fig. 2e). A low charge transfer resistance indicates a significant exchange current density (i^0), which implies an enhancement in the electrochemical activity of SKIER-5. In other words, insertion and deinsertion of the lithium ions during the charge and discharge processes is more favorable. During the subsequent potential sweep from 0.01 to 3.0 V, an increase in the low-frequency charge transfer resistance was observed, accompanied by a more distinct linear region with a 45° angle in the Nyquist plots (Fig. 2f and S14†). This is known as the Warburg element, and it is associated with diffusion phenomena occurring within the particles, which can be described using the Warburg impedance formula.[6]

$$Z_w = A_w(1 - i)\omega^{-1/2} \quad (2)$$

where Z_W represents the impedance, ω is the radial frequency, i is the unit imaginary number, and A_W is the Warburg coefficient, which is inversely proportional to the square root of the diffusion coefficient. An increase in the absolute value of Z_W at a fixed ω indicates an increase in A_W, which suggests a decrease in the diffusion coefficient upon delithiation. A reverse potential sweep from 3.0 to 0.01 V resulted in a reduction of the Warburg element, indicating restoration of the diffusion characteristics (Fig. 2g). Continuous repetition of this activation process gradually increased the number of active sites, leading to a continuous increase in the capacity of SKIER-5 with increasing cycles (Fig. 2h). Fig. 2h shows the typical Nyquist plots recorded during charge/discharge cycles, indicating that the impedance of SKIER-5 continuously decreased. The improvement in impedance was attributed to the gradual activation of SKIER-5, thus gradually converting the whole material

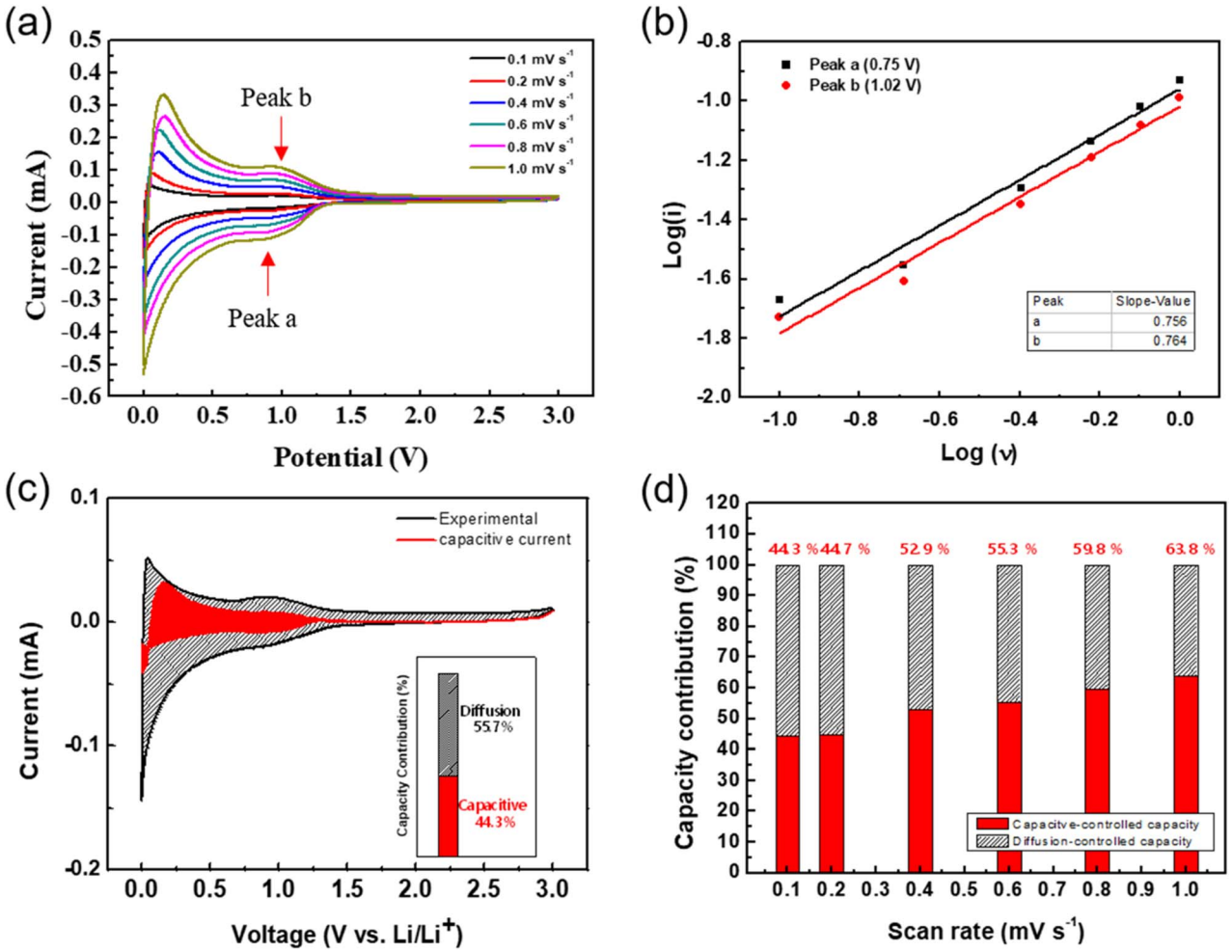

Fig. 3 Dunn method analysis of SKIER-5. (a) CV curves obtained at different scan rates. (b) The corresponding log(*i*) *versus* log(*v*) plots for the two peaks in the CV scans of panel a. (c) Capacitive contribution (red area) at a scan rate of 0.1 mV s^{-1}. (d) Ratio of capacitive contribution (red) at various scan rates.

to the active state. This contributed to the continuous increase in the capacity of SKIER-5 with cycling.

To further study the superior electrochemical performance of the SKIER-5 electrode, the redox kinetics were investigated using a CV experiment to differentiate the capacitive and diffusion-controlled contributions to the total Li^+ storage capacity. The CV profiles were tested with scan rates ranging from 0.1 to 1 mV s^{-1} (Fig. 3a). Previous research has shown that the following equation represents the relationships between current (i) and scan rates (v).[44–47]

$$(i) = av^b \quad (3)$$

$$\log(i) = b\log(v) + \log(a) \quad (4)$$

Variable parameters a and b are used here. A b-value close to 0.5 indicates that the charge/discharge process is mainly controlled by diffusion behavior, whereas a b-value close to 1 suggests that the process is mostly controlled by capacitive behavior. These b-values can be calculated from log(*i*) *versus* log(v) plots. For SKIER-5, the b-values at different oxidation/reduction peaks were 0.756 and 0.764, demonstrating that the redox kinetics of SKIER-5 involved both diffusion and capacitor behaviors (Fig. 3b). Furthermore, capacitive and diffusion-controlled contributions at a specified scan rate were calculated by means of the following equation:

$$i(v) = k_1 v + k_2 v^{0.5} \quad (5)$$

in which k_1 and k_1 represent constants when the voltage is applied. The capacitive and diffusion-controlled contributions were denoted by $k_1 v$ and $k_2 v^{0.5}$, respectively. SKIER-5 showed a capacitive contribution of 55.7% and a diffusion-controlled contribution of 44.3% in total at a scan rate of 0.1 mV s^{-1} (Fig. 3c). Despite the low scan rate, the high capacitive contribution indicated rapid electron and Li^+ transport at the SKIER-5 electrode.

The capacitive contribution (red area) of SKIER-5 at scan rates of 01. 0.2, 0.4, 0.6, 0.8, and 1.0 mV s^{-1} is shown in Fig. S15.† As shown in Fig. 3d, the capacitive contributions were estimated to be 44.7%, 52.9%, 55.3%, 59.8%, and 63.8% at scan

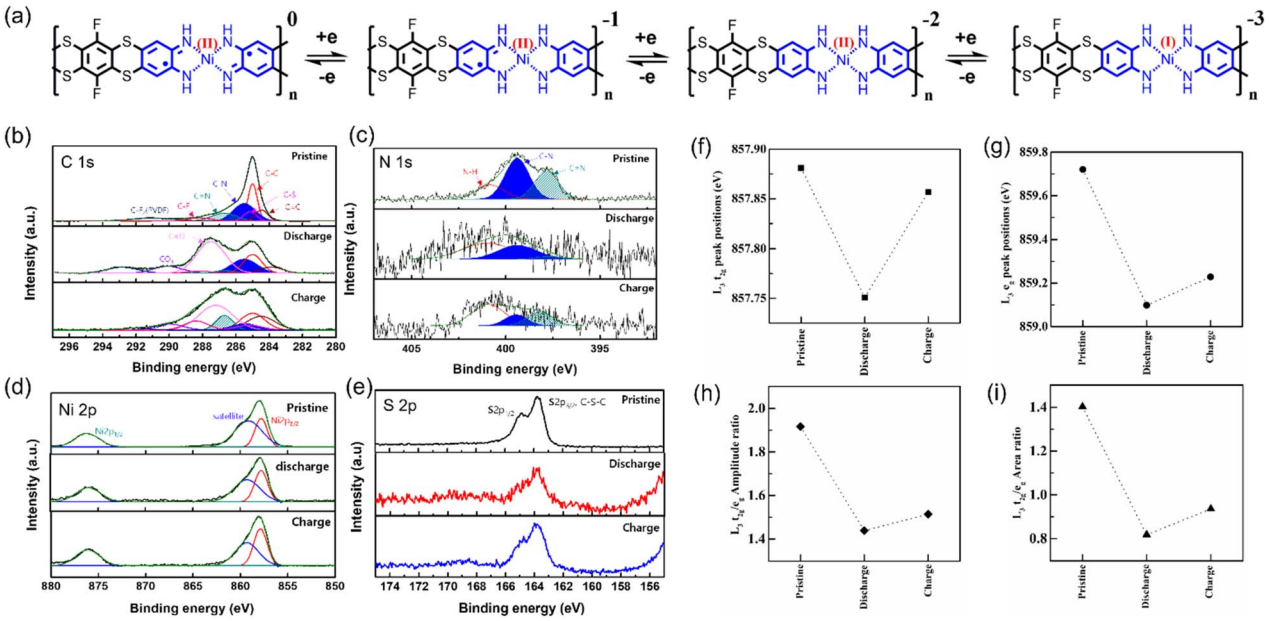

Fig. 4 Charge storage mechanism for SKIER-5. (a) Plausible charge storage mechanism for SKIER-5 (blue and red Ni indicate Ni(II) and Ni(I), respectively). (b) C 1s, (c) N 1s, (d) Ni 2p, and (e) S 2p XPS spectra of SKIER-5; Ni L_3 (f) d_{xy} and (g) $d_{x^2-y^2}$ peak positions, with their (h) amplitudes and (i) area ratios, of the SKIER-5 anode before and after the 1st discharging and charging cycle.

rates of 0.1, 0.2, 0.4, 0.6, 0.8, and 1.0 mV s^{-1}, respectively. Obviously, the capacitive contribution increased significantly with the scan rate, which was advantageous to the rapid transport kinetics of lithium ions and high rate performance lithium ions and high rate performance.

Charge storage mechanism of SKIER-5

The charge storage mechanism of SKIER-5 was found to be comparable to that of Ni(BTA).[6] SKIER-5 underwent three-electron redox reactions during charge/discharge processes within the electrochemical window of 0.01 to 3.0 V (Fig. 4a). In more detail, $TATH^{2-}$ and Ni^{2+} transformed into $TATH^{4-}$ and Ni^{+} by accepting two and one electrons, respectively. To elucidate this mechanism, both ex situ XPS and NEXAFS analyses were conducted. The C 1s XPS spectra showed that the peak assigned to C–N bonds (285.5 eV) increased as that attributed to C=N bonds (286.7 eV) decreased after discharging (Fig. 4b). The N 1s XPS spectra also supported this mechanism. As illustrated in Fig. 4c, the N 1s spectra were deconvoluted into two peaks, indicating C–N bonds (399.6 eV) and C=N bonds (398.2 eV). The intensity of the C=N bond peak clearly decreased after discharge (lithiation). The relative intensity was restored after the material was recharged (delithiation). These results demonstrated that the ligand $TATH^{2-}$ can undergo a two-electron redox process (between $TATH^{2-}$ and $TATH^{4-}$).[6] In the Ni 2p and S 2p XPS spectra (Fig. 4d and e), there were no significant changes during charge/discharge. However, we found evidence for changes in the Ni oxidation number when NEXAFS measurements were carried out.

NEXAFS measurements were carried out on Ni $L_{2,3}$ edges for the SKIER-5 electrode during discharging and charging at the 10D beamline using total electron yield mode. Fig. S16† shows the normalized NEXAFS spectra for the Ni $L_{2,3}$ edges of SKIER-5 after discharging and charging. The spectrum of SKIER-5 exhibited two strong peaks at photon energies of approximately 858 and 876 eV corresponding to the L_3 and L_2 edges, respectively. These edges arose due to the electronic transition to the Ni 3d level from the Ni $2p_{3/2}$ (L3) and Ni $2p_{1/2}$ (L_2) levels. The peaks due to the L_3 and L_2 edges were deconvoluted into two peaks corresponding to t_{2g} and e_g symmetries. Similarly, the peaks attributed to the Ni L_3 and L_2 edges were deconvoluted after the 1st discharge and charging cycle of the electrodes. The changes in the positions of the peaks corresponding to the t_{2g} and e_g symmetries in the L_3 edge were plotted, and the results are shown in Fig. 4f and g. In both cases, it was observed that the peaks shifted to lower energies after discharging and then shifted to higher energies after charging. These changes in the peak positions were attributed due to shifting in either the Ni 3d or 2p orbital due to slight changes in the oxidation states of Ni. A similar trend was observed in the L_3 t_{2g}/e_g amplitude ratio and L_3 t_{2g}/e_g area ratio plots shown in Fig. 4h and i. These changes refer to the changes in the electronic structure during discharging and charging of SKIER-5. *In-situ* FT-IR and XRD, as well as *ex situ* SEM experiments, revealed no notable changes in characteristic bonds, peak positions and morphology of SKIER-5 during the discharge/charge process, respectively (Fig. S17–S19†). These findings indicate the high stability of SKIER-5 during cycling. As a result, it was confirmed that Ni can accept a single electron, being converted from Ni^{2+} to Ni^{+} during a discharge process without undergoing a structural change. Therefore, during charge/discharge cycles, SKIER-5 possibly underwent three-electron redox reactions involving both TATH and Ni(II).

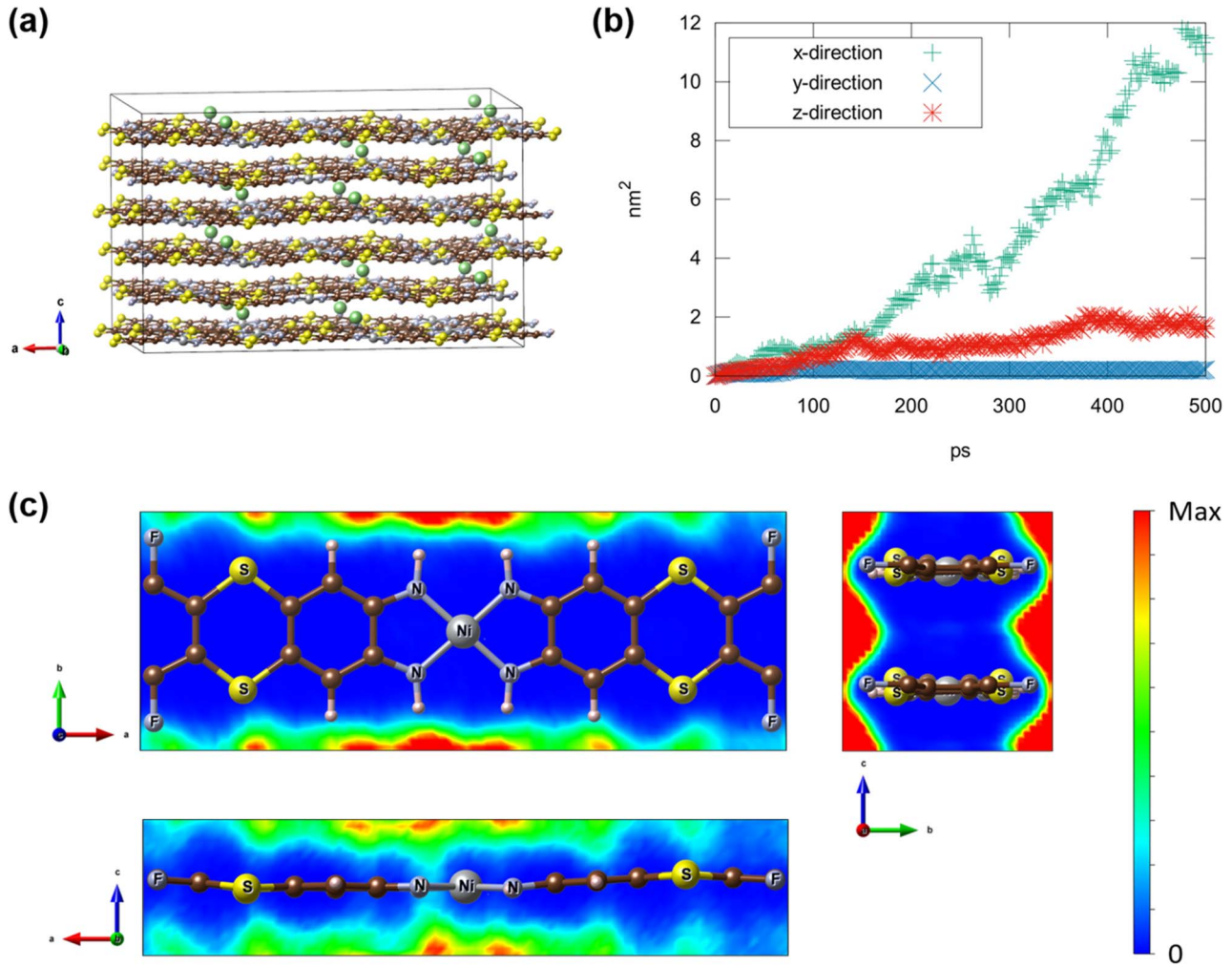

Fig. 5 Molecular dynamics (MD) simulation of SKIER-5. (a) Initial structure of the Li-intercalated SKIER-5 ($Li_{24}C_{864}S_{192}F_{96}N_{192}H_{384}Ni_{48}$) for the molecular dynamics simulation and (b) the calculated mean squared displacement (MSD) over 500 ps at 300 K. (c) The population density map of the relative positions of Li ions from each Ni site in SKIER-5.

To elucidate the excellent electron-accommodating capability of SKIER-5, we modeled several non-periodic structures by replacing the sulfur moiety of the thianthrene group with oxygen, nitrogen, or carbon. Using the DFT method, we calculated the energy levels and spatial distributions of the lowest unoccupied molecular orbital (LUMO) for these modeled structures. Among various model structures examined, Ni(TATH) with the sulfur moiety exhibited the lowest LUMO level of −3.22 eV, enabling a relatively favorable electron accommodation (Fig. S20†). Furthermore, this low LUMO level in SKIER-5 contributes to enhancing the reduction stability of electrolytes[48,49] and improving electronic conductivity.[50] Therefore, the ability of SKIER-5 to readily accommodate electrons through three-electron redox reactions involving both TATH and Ni(II) has motivated us to explore its potential as an anode with low activation energy at low temperatures.

To identify the pathways of Li diffusion within SKIER-5, we employed classical molecular dynamics (MD) simulations utilizing the LAMMPS package[51] with UFF4MOF[52] interatomic potentials. To model the Li diffusion within SKIER-5, 24 Li ions were introduced into the super-cell of the crystalline SKIER-5 structure, which comprises 24 polymer chains per cell (Each chain contains two Ni ions in the super-cell). The resulting structure was converted into a LAMMPS input file using the LAMMPS-interface code.[53] While classical MD simulations cannot explicitly capture charge exchange between ions, our approach yielded and optimized Li-intercalated structure similar to the DFT result, validating its effectiveness. To track the Li movement, we conduct MD simulations at 300 K for 500 ps using NVT ensemble with a 2 fs time step. The calculated mean squared displacement (MSD) of Li ions revealed significant diffusion along the polymer chains (*x*-direction in Fig. 5b and ESI†), with minimal diffusion in other directions, particularly in the *y*-direction. The population density map of Li-ion position relative to each Ni-ion (Fig. 5c), obtained from the MD simulation (from 100 ps to 500 ps), demonstrate that the preferred Li-intercalation sites are near N atoms, followed by S and F. Along with MD simulation, DFT calculations identified

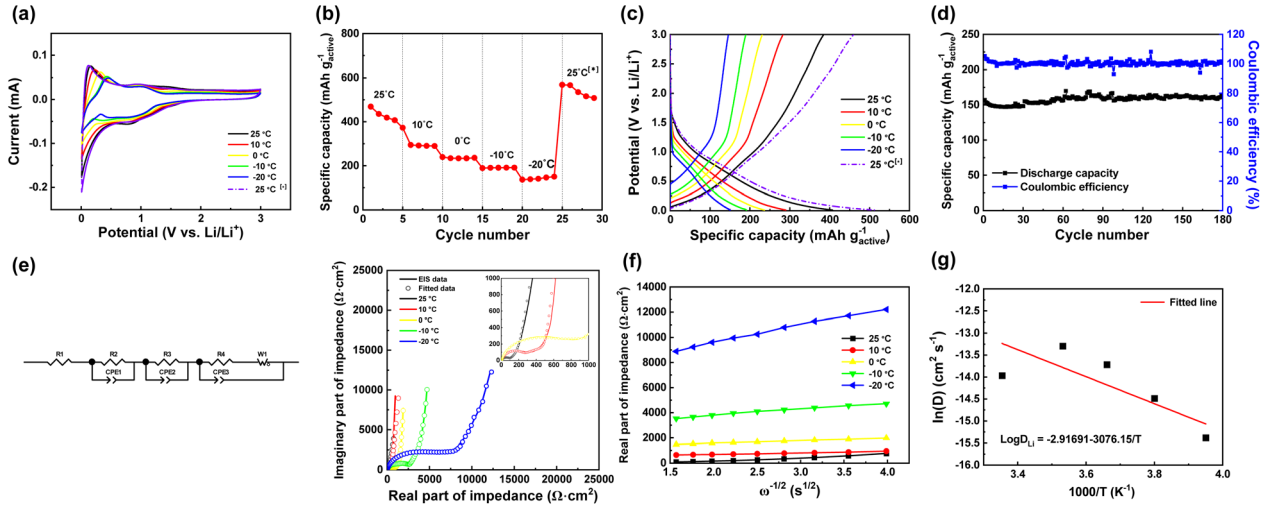

Fig. 6 Low-temperature electrochemical performance of SKIER-5 electrode half cells at various temperatures from 25 to −20 °C. (a) Initial CV curves of SKIER-5 obtained at a scan rate of 0.1 mV s^{-1}. (b) Temperature-dependent galvanostatic cycling of SKIER-5 at 113 mA g^{-1} (0.2C). (c) 5th cycle discharge–charge curves of SKIER-5. (d) Changes in specific capacity and coulombic efficiency of SKIER-5 over 180 cycles at −20 °C with a current density of 113 mA g^{-1} (0.2C). (e) Electrochemical impedance spectroscopy (EIS) of SKIER-5 at various temperatures from 25 to −20 °C. (f) Graph of Z_{Re} *versus* $\omega^{-1/2}$ for the low-frequency section of fig. 6e. (g) Linear relationship between ln D and $10^3/T$ at different temperatures (25 °C [*] indicates that the temperature was returned to 25 °C).

three Li binding sites: two tetra-amine sites and one S–F site (Fig. S21†). In the initial charging state, the tetra-amines with delocalized π orbital can bind 4 Li ions per unit formula. Subsequently, in the fully charged state, the electron-rich S–F sites can additionally bind 10 Li ions per unit formula, achieving a theoretical capacity of 743 mA h g^{-1} (Fig. S22†).

Low-temperature electrochemical performance of SKIER-5

The performance of the SKIER-5 electrode at low temperatures was evaluated through various tests such as CV measurements, galvanostatic discharge–charge, rate performance, and cycling tests (Fig. 6). Fig. 6a illustrates the CV curves obtained at different temperatures (ranging from 25 to −20 °C) for potentials of 0.01–3.0 V *vs.* Li/Li^+ and a scan rate of 0.1 mV s^{-1}. At 25 °C, two pairs of cathodic/anodic peaks were observed. However, as the temperature was decreased, the cathodic peak at 1.4 V *vs.* Li/Li^+ disappeared and the cathodic peak at 0.79 V *vs.* Li/Li^+ shifted to 0.87 V *vs.* Li/Li^+. Similar behavior was observed for the anodic peaks; the peak at 1.41 V *vs.* Li/Li^+ disappeared, and the anodic peak at 0.96 V *vs.* Li/Li^+ shifted to 1.01 V *vs.* Li/Li^+. Consequently, only one pair of cathodic/anodic peaks was observed between 0 °C and −20 °C. Fig. 6b presents the discharge capacities of SKIER-5 at different temperatures ranging from 25 to −20 °C, with a current density of 0.2C. At 25 °C, the discharge capacity of SKIER-5 was 407.16 mA h g^{-1}. However, at temperatures of 10, 0, −10, and −20 °C, the discharge capacities decreased to 289.81, 236.19, 191.38, and 150.30 mA h g^{-1}, respectively, which corresponded to 71.2%, 58.0%, 47.0%, and 36.9% of the initial capacity seen at 25 °C. Table 1 and Fig. S23† shows the discharge capacities and the electrochemical performance of commercial graphite (Artificial graphite, LiBest Inc.) under the same conditions. The discharge capacities of SKIER-5 were significantly higher than those of the commercial graphite at low temperatures (<−10 °C), and the discharge capacity of SKIER-5 was approximately five times higher than that of commercial graphite at −20 °C. Additionally, SKIER-5 maintained an excellent specific capacity (508.46 mA h g^{-1} at 0.2C) after returning to 25 °C. Even compared to graphite electrodes with a high content of Super P (50 wt%), the discharge capacity of the SKIER-5 electrode was higher than that of the commercial graphite electrode at −20 °C with approximately twice the capacity retention (Fig. S24 and Table S4†). The poor dynamic conditions for the lithium ions at low temperatures caused the commercial graphite anode to

Table 1 Comparison of the cyclic performance (mAh g^{-1}_{active}) of SKIER-5 and commercial graphite at 0.2C at different temperatures ranging from 25 °C to −20 °C (0.2C = 113 mA g^{-1} for SKIER-5 and 0.2C = 74.4 mA g^{-1} for commercial graphite)

	Discharge capacity (mAh g^{-1} active) at various temperature					
Electrodes	25 °C	10 °C	0 °C	−10 °C	−20 °C	25 °C
SKIER-5	407.16 (100%)[a]	289.81 (71.2)	236.19 (58.0)	191.38 (47.0)	150.30 (36.9)	508.46 (124.8)
Commercial graphite	367.77 (100%)	307.72 (83.7)	156.31 (42.5)	72.61 (19.7)	28.58 (7.8)	374.87 (101.9)

[a] The numbers in brackets represent the percentages of the capacity at 25 °C.

Table 2 Fitted results from EIS at various temperatures

	25 °C	10 °C	0 °C	−10 °C	−20 °C
R_{ct}/Ω	96.85	364.2	883.71	2577.3	6254.45
R_b/Ω	3.75	5.67	6.95	9.28	13.36
$D_{Li}/cm^2\ s^{-1}$	2.057×10^{-13}	9.666×10^{-13}	3.668×10^{-13}	6.228×10^{-14}	7.913×10^{-15}

experience reduced lithium insertion rates, resulting a significant decrease in capacity. These results demonstrated that SKIER-5 has better low-temperature capacity retention during cycling and better capacity recovery than commercial graphite due to its stable structure, and lower activation energy for charge transfer. Furthermore, the high capacitive contribution of SKIER-5 facilitated Li^+ transmission at low temperatures. Fig. 6c shows the 5th galvanostatic discharge–charge curves of the SKIER-5 electrode at temperatures ranging from −20 °C to 25 °C. When the temperature was increased back to 25 °C, the curve almost overlapped with the initial 25 °C curve, indicating no loss in capacity. Fig. 6d shows that after 180 cycles at −20 °C and 0.2C, SKIER-5 maintained a high specific capacity of 163 mA h g^{-1} without any capacity degradation. These findings were consistent with the CV results shown in Fig. 6a, which confirmed the exceptional adaptability of SKIER-5 in low-temperature conditions.[54]

To understand the electrode impedance of the SKIER-5 anode, electrochemical impedance spectroscopy was carried out at frequencies from 100 kHz to 0.01 Hz and different temperatures ranging from 25 to −20 °C, and the equivalent circuit used is shown in Fig. 6e. The equivalent circuit includes R1 (R_b), R2, R3, and R4 (R_{ct}). R1 (R_b) represents the bulk resistance of the SKIER-5 electrode. R2, R3, and R4 (R_{ct}) correspond to the charge transfer resistances of the lithium metal, the SEI layer, and SKIER-5, respectively. CPE1, CPE2, and CPE3 denote the constant phase-angle elements, involving the double layer capacitance, of the lithium metal, the SEI layer, and SKIER-5. W1 (Z_w) represents the linear Warburg element in the low-frequency range, related to the impedance of Li^+ diffusion within the SKIER-5 electrode.[55–57] The fitted results are presented in Table 2. The lithium ion diffusion coefficient (D_{Li}) is related to the Li^+ diffusion process within the SKIER-5 electrode, which can be calculated from the Nyquist plot of the low-frequency section using the following equations:

$$Z_{Re} = R_{ct} + R_b + \sigma\omega^{-1/2} \quad (6)$$

$$D_{Li} = \frac{R^2T^2}{2A^2n^4F^4C_{Li}^2\sigma^2} \quad (7)$$

where ω represents the angular frequency, R is the gas constant, A is the electrode surface area, T is the absolute temperature, F is the Faraday constant, n refers to the number of electrons transferred in the half-reaction for the redox couple, and C_{Li} represents the concentration of lithium ions in the electrolyte (2.0×10^{-4} mol cm^{-3}). σ is the Warburg factor relative to Z_{Re} *vs.* $\omega^{-1/2}$ and was calculated from the slope of the lines in Fig. 6f. The calculated values of σ were 269.53 at 25 °C, 124.36 at 10 °C, 201.88 at 0 °C, 489.93 at −10 °C, and 1374.46 at −20 °C. Using these values, the lithium ion diffusion coefficients were calculated and the results are presented in Table 2. SKIER-5 exhibited low transfer resistance (R_{ct}) and high lithium ion diffusion (D_{Li}) at temperatures ranging from 25 to −20 °C. The relationship between the diffusion coefficient (D) and temperature (T) can be expressed with the Arrhenius equation:

$$D = D_0 e^{-\frac{E_a}{k_B T}} \quad (8)$$

where D_0 is the diffusion constant and E_a is the activation energy for diffusion, both of which depend on the composition and structure of the materials and are independent of temperature. k_B is the Boltzmann constant ($k_B = 1.3806505(24) \times 10^{-23}$ J K^{-1}). We took the natural logarithms of both sides of the Arrhenius equation to obtain the equation:

$$\ln D = \ln D_0 - \frac{E_a}{k_b T} \quad (9)$$

The relationship between ln D and $10^3/T$ is shown in Fig. 6g. The slope of the fitted line was used to estimate the diffusion activation energy E (approximately 0.23 eV), which was lower than that of graphite (~0.6 eV).[11] This suggests that SKIER-5 has a relatively low activation energy for Li^+ diffusion and undergoes fast surface faradaic reactions.

Conclusions

In summary, this work presents the design and synthesis of redox-active fluoro-thianthrene-based MOFs and their electrochemical properties as anodes for LIBs at various temperatures. SKIER-5 is unambitiously characterized by powder XRD, XPS, XANES, EXAFS, solid-state ^{13}C NMR and FT-IR analysis. TATH with the delocalized π orbital of the tetraamine ligand coordinated to Ni(II) in a square planar manner, resulting in a one-dimensional linear structure. CV scans revealed the charge/discharge storage mechanism of the SKIER-5 anode as resulting from equal contributions from redox-rich diffusion and capacitive behavior. Notably, the capacity considerably increased during the cycling charge/discharge process because of the formation of more active sites in the redox process. After 1600 cycles, the capacity reached 600 mA h g^{-1}, comparable or superior to those of MOFs used for lithium-ion batteries. Such a high capacity was attributed to the three-electron redox properties of both TATH and Ni, as confirmed by XPS and NEXAFS analysis. In addition, the exceptional electron-accommodating capability of SKIER-5 was elucidated by its low LUMO level of −3.22 eV, as determined through DFT calculations for the non-periodic model structure. Most

importantly, SKIER-5 exhibited significantly higher discharge capacities than commercial graphite at low temperatures (<−10 °C) because of a lower activation energy (~0.23 eV) for charge transfer. Moreover, it maintained stability when cycled at −20 °C, highlighting its potential as a promising anode material in low-temperature environments.

Data availability

The data supporting this article have been included as part of the ESI.†

Author contributions

Y. K. and H. K. conceived the idea. Y. K., T. H. K., I. S., W. D., S. O. H., J. Y. and H. K. wrote the manuscript. S. B., S. N. and K. H. C. performed the synchrotron *in situ* XRD, NEXAFS and XAFS experiments. K. Y. and S. L. performed the DFT calculations. T. H. K., B. K., S. K and J. Y. performed the electrochemical experiments. Y. K. synthesized the materials. All authors discussed the results and approved the final version of the manuscript.

Conflicts of interest

There are no conflicts to declare.

Acknowledgements

This study was supported by the Center for Advanced Meta-Materials (CAMM), which is funded by the Korean Ministry of Science and Information and Communication Technologies (MSIT) as a Global Frontier Program (2019M3A6B3030636). This work was also conducted within the framework of the Research and Development Program of the Korea Institute of Energy Research (C4−2410). X-ray diffraction studies with synchrotron radiation were performed at the Pohang Accelerator Laboratory (Beamline 1D, 2D and 10D) supported by MSIT and POSTECH. This research was also partially supported by the National Research Council of Science & Technology grant by the Korean government (MSIT) (No. CAP22073-000); and the Development of high-power capacitor (supercapacitor) performance enhancement technology customized for companies by the Ministry of Trade, Industry and Energy and Korea Evaluation Institute of Industrial Technology [Project No. 00155725/Project Name: Development of battery capacitors for long-term, high-capacity, and high power energy storage system].

References

1 J. Calbo, M. J. Golomb and A. Walsh, *J. Mater. Chem. A*, 2019, **7**, 16571–16597.
2 K. Fan, C. Zhang, Y. Chen, Y. Wu and C. Wang, *Chem*, 2021, **7**, 1224–1243.
3 R. A. Kharod, J. L. Andrews and M. Dincă, *Annu. Rev. Mater. Res.*, 2022, **52**, 103–128.
4 G. Zhang, L. Jin, R. Zhang, Y. Bai, R. Zhu and H. Pang, *Coord. Chem. Rev.*, 2021, **439**, 213915.
5 L. Sun, M. G. Campbell and M. Dincă, *Angew. Chem., Int. Ed.*, 2016, **55**, 3566–3579.
6 R. R. Kapaev, S. Olthof, I. S. Zhidkov, E. Z. Kurmaev, K. J. Stevenson, K. Meerholz and P. A. Troshin, *Chem. Mater.*, 2019, **31**, 5197–5205.
7 W. Yin, G. Zhang, X. Wang and H. Pang, *Adv. Colloid Interface Sci.*, 2021, **298**, 102562.
8 M. Li, J. Lu, Z. Chen and K. Amine, *Adv. Mater.*, 2018, **30**, 1800561.
9 X. Yao, J. Kong, D. Zhou, C. Zhao, R. Zhou and X. Lu, *Carbon*, 2014, **79**, 493–499.
10 A. Gupta and A. Manthiram, *Adv. Energy Mater.*, 2020, **10**, 2001972.
11 K. Xu, A. von Cresce and U. Lee, *Langmuir*, 2010, **26**, 11538–11543.
12 A. Belgibayeva, A. Rakhmetova, M. Rakhatkyzy, M. Kairova, I. Mukushev, N. Issatayev, G. Kalimuldina, A. Nurpeissova, Y.-K. Sun and Z. Bakenov, *J. Power Sources*, 2023, **557**, 232550.
13 J. Kim, H. Kim, S. Lee, G. Kwon, T. Kang, H. Park, O. Tamwattana, Y. Ko, D. Lee and K. Kang, *J. Mater. Chem. A*, 2021, **9**, 14485–14494.
14 Z. Liu, F. Zheng, W. Xiong, X. Li, A. Yuan and H. Pang, *SmartMat*, 2021, **2**, 488–518.
15 J. Yan, Y. Cui, M. Xie, G.-Z. Yang, D.-S. Bin and D. Li, *Angew. Chem., Int. Ed.*, 2021, **60**, 24467–24472.
16 J. Xie, Z. Wang, Z. J. Xu and Q. Zhang, *Adv. Energy Mater.*, 2018, **8**, 1703509.
17 X.-F. Cheng, J. Li, X. Hou, J. Zhou, J.-H. He, H. Li, Q.-F. Xu, N.-J. Li, D.-Y. Chen and J.-M. Lu, *Sci. China: Chem.*, 2019, **62**, 753–760.
18 A. Wild, M. Strumpf, B. Häupler, M. D. Hager and U. S. Schubert, *Adv. Energy Mater.*, 2017, **7**, 1601415.
19 W. J. Ong and T. M. Swager, *Nat. Chem.*, 2018, **10**, 1023–1030.
20 S. Bai, B. Kim, C. Kim, O. Tamwattana, H. Park, J. Kim, D. Lee and K. Kang, *Nat. Nanotechnol.*, 2021, **16**, 77–84.
21 D. J. Kim, D.-J. Yoo, M. T. Otley, A. Prokofjevs, C. Pezzato, M. Owczarek, S. J. Lee, J. W. Choi and J. F. Stoddart, *Nat. Energy*, 2019, **4**, 51–59.
22 M. Kolek, F. Otteny, P. Schmidt, C. Mück-Lichtenfeld, C. Einholz, J. Becking, E. Schleicher, M. Winter, P. Bieker and B. Esser, *Energy Environ. Sci.*, 2017, **10**, 2334–2341.
23 M. Lee, J. Hong, H. Kim, H.-D. Lim, S. B. Cho, K. Kang and C. B. Park, *Adv. Mater.*, 2014, **26**, 2558–2565.
24 Z. Lin, H.-Y. Shi, L. Lin, X. Yang, W. Wu and X. Sun, *Nat. Commun.*, 2021, **12**, 4424.
25 R. Shi, L. Liu, Y. Lu, C. Wang, Y. Li, L. Li, Z. Yan and J. Chen, *Nat. Commun.*, 2020, **11**, 178.
26 M. E. Speer, M. Kolek, J. J. Jassoy, J. Heine, M. Winter, P. M. Bieker and B. Esser, *Chem. Commun.*, 2015, **51**, 15261–15264.
27 Y.-Y. Wang, M. Zhang, S.-L. Li, S.-R. Zhang, W. Xie, J.-S. Qin, Z.-M. Su and Y.-Q. Lan, *Chem. Commun.*, 2017, **53**, 5204–5207.
28 G. Friedel, *Bulletin de Minéralogie*, 1907, **30**, 326–455.

29 B. Ravel and M. Newville, *J. Synchrotron Radiat.*, 2005, **12**, 537–541.
30 G. Kresse and J. Hafner, *Phys. Rev. B*, 1993, **47**, 558–561.
31 J. P. Perdew, K. Burke and M. Ernzerhof, *Phys. Rev. Lett.*, 1996, **77**, 3865–3868.
32 S. Grimme, J. Antony, S. Ehrlich and H. Krieg, *J. Chem. Phys.*, 2010, **132**, 154104.
33 L. Wang, T. Maxisch and G. Ceder, *Phys. Rev. B*, 2006, **73**, 195107.
34 Y. Youn, M. Lee, C. Hong, D. Kim, S. Kim, J. Jung, K. Yim and S. Han, *Comput. Phys. Commun.*, 2020, **256**, 107450.
35 G. Cai, P. Cui, W. Shi, S. Morris, S. N. Lou, J. Chen, J.-H. Ciou, V. K. Paidi, K.-S. Lee, S. Li and P. S. Lee, *Advanced Science*, 2020, **7**, 1903109.
36 Q. Zhao, D. Zhu, X. Zhou, S.-H. Li, X. Sun, J. Cui, Z. Fan, M. Guo, J. Zhao, B. Teng and B. Cheng, *ACS Appl. Mater. Interfaces*, 2021, **13**, 52960–52966.
37 C. G. Silva, A. Corma and H. García, *J. Mater. Chem.*, 2010, **20**, 3141–3156.
38 A. Bravais, *Etudes Cristallographiques*, Gauthier-Villars, 1866.
39 J. D. H. Donnay and D. Harker, *Am. Mineral.*, 1937, **22**, 446–467.
40 S. Zheng, X. Li, B. Yan, Q. Hu, Y. Xu, X. Xiao, H. Xue and H. Pang, *Adv. Energy Mater.*, 2017, **7**, 1602733.
41 W. Choi, J. Ha, Y.-T. Kim and J. Choi, *ChemSusChem*, 2022, **15**, e202201137.
42 Y. S. Choi, W. Choi, W.-S. Yoon and J. M. Kim, *ACS Nano*, 2022, **16**, 631–642.
43 T. Kim, S. Kang, S. Park, C.-W. Lee, S. Iyan, B. Kim, J. Baek, H.-J. Choi, H. Kim and J. Yoo, *J. Power Sources*, 2024, **603**, 234449.
44 Q. Su, X. Cao, T. Yu, X. Kong, Y. Wang, J. Chen, J. Lin, X. Xie, S. Liang and A. Pan, *J. Mater. Chem. A*, 2019, **7**, 22871–22878.
45 X. Hu, X. Liu, K. Chen, G. Wang and H. Wang, *J. Mater. Chem. A*, 2019, **7**, 11016–11037.
46 H. Wan, G. Liu, Y. Li, W. Weng, J. P. Mwizerwa, Z. Tian, L. Chen and X. Yao, *ACS Nano*, 2019, **13**, 9551–9560.
47 Q. Zhang, Z. Ding, G. Liu, H. Wan, J. P. Mwizerwa, J. Wu and X. Yao, *Energy Storage Mater.*, 2019, **23**, 168–180.
48 Z. Li, R. Yu, S. Weng, Q. Zhang, X. Wang and X. Guo, *Nat. Commun.*, 2023, **14**, 482.
49 J.-G. Han, J. B. Lee, A. Cha, T. K. Lee, W. Cho, S. Chae, S. J. Kang, S. K. Kwak, J. Cho, S. Y. Hong and N.-S. Choi, *Energy Environ. Sci.*, 2018, **11**, 1552–1562.
50 G. Liu, S. Xun, N. Vukmirovic, X. Song, P. Olalde-Velasco, H. Zheng, V. S. Battaglia, L. Wang and W. Yang, *Adv. Mater.*, 2011, **23**, 4679–4683.
51 A. P. Thompson, H. M. Aktulga, R. Berger, D. S. Bolintineanu, W. M. Brown, P. S. Crozier, P. J. in 't Veld, A. Kohlmeyer, S. G. Moore, T. D. Nguyen, R. Shan, M. J. Stevens, J. Tranchida, C. Trott and S. J. Plimpton, *Comput. Phys. Commun.*, 2022, **271**, 108171.
52 D. E. Coupry, M. A. Addicoat and T. Heine, *J. Chem. Theory Comput.*, 2016, **12**, 5215–5225.
53 P. G. Boyd, S. M. Moosavi, M. Witman and B. Smit, *J. Phys. Chem. Lett.*, 2017, **8**, 357–363.
54 C. Huang, S.-X. Zhao, H. Peng, Y.-H. Lin, C.-W. Nan and G.-Z. Cao, *J. Mater. Chem. A*, 2018, **6**, 14339–14351.
55 T. Yuan, X. Yu, R. Cai, Y. Zhou and Z. Shao, *J. Power Sources*, 2010, **195**, 4997–5004.
56 S.-L. Chou, J.-Z. Wang, H.-K. Liu and S.-X. Dou, *J. Phys. Chem. C*, 2011, **115**, 16220–16227.
57 H. Ge, L. Cui, B. Zhang, T.-Y. Ma and X.-M. Song, *J. Mater. Chem. A*, 2016, **4**, 16886–16895.